Journal of Alloys and Compounds 960 (2023) 170683

Contents lists available at ScienceDirect

Journal of Alloys and Compounds

journal homepage: www.elsevier.com/locate/jalcom

Low-operational temperature for selective detection of xylene gas using a p-n CuO-ZnO heterostructure-based sensor

Lekgolo M. Maebana [a], Rapelang G. Motsoeneng [b], Zamaswazi P. Tshabalala [b], Hendrik C. Swart [b], Franscious R. Cummings [c], Mudalo Jozela [d], Steven S. Nkosi [a], David E. Motaung [b,*]

[a] Department of Physics, University of Limpopo, Private Bag X1106, Sovenga 0727, South Africa
[b] Department of Physics, University of the Free State, P.O. Box 339, Bloemfontein ZA9300, South Africa
[c] Electron Microscope Unit, University of the Western Cape, Robert Sobukwe Road, Bellville 7535, South Africa
[d] National Metrology Institute of South Africa (NMISA), CSIR Campus, Building 5, Meiring Naude Road, Brummeria, Pretoria 0182, South Africa

ARTICLE INFO

Article history:
Received 31 January 2023
Received in revised form 19 May 2023
Accepted 20 May 2023
Available online 22 May 2023

Keywords:
CuO
ZnO
Xylene
Gas sensor
Heterostructure

ABSTRACT

Xylene is not just considered detrimental to the environment but also hazardous to humans. Herein we report on xylene vapour detection using CuO-ZnO heterostructures containing various concentrations (0.1–2.0 wt%) of Zn, prepared via hydrothermal synthesis. X-ray diffraction, scanning, and transmission electron microscopy, as well as x-ray photoelectron spectroscopy, validated the formation of the CuO-ZnO heterostructure. Gas detection, sensitivity, selectivity, and stability tests of nine different gases, namely benzene, toluene, ethylbenzene, xylene, ethanol, methane, SO_2, NO_2, and CO_2 at various operational temperatures were subsequently investigated. It was found that a CuO-ZnO heterostructure with 1.0 wt% Zn showed excellent selectivity towards 100 ppm of xylene at 100 °C. The sensor further demonstrated an insignificant cross-sensitivity ($S_{xylene}/S_{toluene}$= 2.7) and ($S_{xylene}/S_{benzene}$ = 8.5) towards toluene and benzene vapour. Additionally, the ultra-low limit of detection of 9.5 ppb and sensitivity of 0.063 ppm^{-1} were observed towards xylene vapour, which indicated that the CuO-ZnO (1.0 wt%) heterostructure-based sensor can realize sub-ppb-level xylene concentration. The sensor disclosed excellent long-term stability in dry air and 40% relative humidity. The superior gas sensing characteristics could be ascribed to the superior surface area, the creation of p-n heterojunction, the robust chemical affinity, and the catalytic performance of p-type CuO on xylene vapour. The response mechanism towards xylene was also clarified.

1. Introduction

With the rapid advancement of urbanization and industrialization over the years, monitoring outdoor and indoor pollution has become an important focal point for the science community as worsening air pollution has strongly affected human health. Globally, about 4 million people die annually because of poor air quality [1]. Amongst the volatile organic compounds (VOCs), benzene, toluene, ethylbenzene, and xylene (BTEX) are hazardous aromatic hydrocarbon compounds, which have become chronic environmental air polluters. These compounds are mostly utilized as organic solvents in factories of paint, leather, plastic, etc, however, it is also well-known that the use of heaters during the cold seasons to warm up indoor spaces tends to release significant amounts of BTEX [2]. Among the BTEX complexes, xylene is the most common indoor pollutant, with prolonged exposure having serious consequences for the human respiratory system [3,4]. While several methods have been attempted to detect or monitor xylene vapour, they appear to be expensive to operate and maintain [5,6]. Thus, cheaper methods that selectively, accurately, and rapidly detect and monitor xylene vapour are urgently required.

Xylene gas sensors using various semiconductor metal oxides (SMOs) are well-reported [7–12]. Guo et al. [13] fabricated a SnO_2-Co_3O_4 heterostructure-based sensor for selective detection of xylene at 100 ppm at 175 °C. Wang et al. [14] fabricated SnO_2/Co_3O_4 nanorods-based sensors for the detection of 100 ppm xylene at an operational temperature of 280 °C. Kim et al. [15] developed Cr_2O_3/$ZnCr_2O_4$ heterostructure-based sensor to detect 5 ppm xylene at 275 °C using a galvanic replacement reaction. Chan et al. [16] prepared a Fe_2O_3-$ZnFe_2O_4$ composite sphere-based sensor, which

* Corresponding author.
E-mail address: MotaungDE@ufs.ac.za (D.E. Motaung).

https://doi.org/10.1016/j.jallcom.2023.170683
0925-8388/

displayed vastly sensitive detection to 5 ppm xylene at an elevated temperature of 300 °C. Elsewhere, p-p-type $NiO/NiCr_2O_4$ heterostructures fabricated using a hydrothermal synthesis displayed a superior selectivity towards xylene, with minimal cross-sensitivity towards other interferences at the operational temperature of 225 °C [17]. A recent report by Li et al. [18] showed rapid response/recovery behaviour towards xylene using $ZnCo_2O_4$ hierarchical porous architectures-based sensor at an operational temperature of 260 °C. As shown, significant work has been done on xylene detection, with the sensors disclosing a rapid response and recovery times. However, the elevated sensing temperatures pose new challenges to these SMO-based sensors. Such high operating temperatures lead to higher power consumption and poor long-term stability. It is found that elevated operational temperature leads to the growth of SMO grains, thus influencing the gas diffusion at the grain boundaries that is accountable for the unwanted long-term drift issue induced by sintering [19,20]. Therefore, the present study reports on the selective detection of xylene, as an indoor air pollutant, at a low operational temperature of 100 °C, utilizing p-n CuO-ZnO heterostructure-based sensors prepared using a hydrothermal approach. The mechanism for improved xylene sensing characteristics was also deliberated from the synergistic influence of oxygen vacancies (V_O) and the creation of p-n CuO-ZnO heterostructure.

2. Experimental details

2.1. Materials

All the reagents were utilized without any additional purification. Zinc (II) acetate dihydrate ($Zn\ (CH_3COO)_2.2\ H_2O$) (> 98% purity), copper (II) acetate monohydrate ($C_4\ H_6CuO_4{\cdot}H_2O$, > 98%), ethanol, and sodium hydroxide (NaOH,) were purchased from Merck. Nine (9) primary reference gas mixtures (PRGMs) were used to test the fabricated sensor devices. The PRGMs were purchased from the National Metrology Institute of South Africa (NMISA) with a cylinder capacity of 5 L. These included toluene, ethylbenzene, and xylene (BTEX), ethanol, methane (CH_4), sulphur dioxide (SO_2), carbon dioxide (CO_2), and nitrogen dioxide (NO_2).

2.2. Synthesis of CuO-ZnO heterostructures

In a typical 250 mL Erlenmeyer flask, 2.5 g $C_4H_6CuO_4{\cdot}H_2O$ and different ratios (0.1, 0.25, 0.5, 1.0, and 2.0 wt%) of $Zn\ (CH_3COO)_2.2\ H_2O$ were added respectively. Equal amounts (40 mL) of water and ethanol were also added to dissolve the precursors. A 0.5 M NaOH was gradually added to the mixture using a pipette and the solution was stirred for 1 h. Finally, the mixture was transferred into a lined autoclave Teflon vessel for 1 h at 150 ºC. Then, the precipitates were washed with ethanol and water, then dried at 80 ºC in the oven, and calcined at 400 °C for 2 h.

2.3. Characterization techniques

The structural characteristics were investigated utilizing X-ray diffraction (XRD, Bruker AXS D8 Advance x-ray diffractometer) fitted with a Cu-kα x-ray radiation source. A scanning electron microscope (SEM, Zeiss) was employed to investigate the surface morphology. Structural and morphological analyses were done by high-resolution transmission electron microscope imaging (HR-TEM, FEI Tecnai G^2 20 FEG-TEM operated at 200 kV) and selected area electron diffraction (SAED) analysis. Spectral image (SI) maps of the different SMOs were collected by coupling the STEM probe with energy dispersive x-ray spectroscopy (EDS); so-called (STEM-EDS). A Micromeritics Tristar 3000 analyzer was used to measure the surface areas and N_2-adsorption/desorption isotherms utilizing the Barrett Emmett–Teller (BET) instrument. The elemental composition measurements were conducted using x-ray photoelectron spectroscopy (PHI 5000 Scanning ESCA Microprobe).

2.4. Sensing device fabrication and measurements

To prepare and fabricate CuO-ZnO-based sensors, the nanomaterials were mixed with ethanol and grinded in a mortar to form a paste, which was homogenously spread over the interdigital electrodes. The variation in the resistance of the sensors was measured by using a 4-channel Gas Mixing System (GMS) sensing station. The assembled sensing devices were placed in a chamber made of Teflon and exposed to nine different gases, which included BTEX, ethanol, CH_4, SO_2, CO_2, and NO_2. The measurements were conducted at four operational temperatures (25, 75, 100, and 150 °C). The sensors' temperatures were set by altering the heating voltage. Prior to the measurements, the sensors were exposed to dry air for 3 hrs to stabilize the resistance and during the measurements, the sensors were tested to analyte gases for 5 min, and the dry air was also introduced for 5 min for recovery. The sensing response was specified as R_g/R_a and R_a/R_g, for the reducing and oxidizing gas, respectively, denoting the resistance ratio of the sensor exposed to air (R_a) and tested gases (R_g).

3. Structural and morphological measurements

Fig. 1**(a)** illustrates the XRD patterns of the CuO-ZnO heterostructures synthesized by varying the concentrations of Zn^{2+} on the CuO matrix. For the Zn (0.1 wt%) in CuO, the patterns indeed confirm the formation of CuO-ZnO heterostructure, where the (100), (002), (101), (102), and (110) planes associated with ZnO structure are observed. These peaks are also observed at higher concentrations (i.e., 0.25–1.0 wt%) of Zn. Moreover, peaks associated with CuO are also observed. Nonetheless, when increasing the concentration of Zn, the (111) and (200) peaks associated with CuO became broad and their intensity reduced for the CuO-ZnO (1.0 wt%). Additionally, the intensity of the (100), 002) and (101) peaks associated with ZnO increased for the CuO-ZnO (1.0 wt%) heterostructure.

A shifting of the CuO (111) peak to lower angles and a reduction in peak intensity are also witnessed when increasing the Zn content (0.1–1 wt%) on the CuO matrix, see Fig. 1**(b)**. This shift could be associated with a higher ionic radius of Zn^{2+} (0.74 Å) in comparison to that of Cu^{2+} (0.73 Å) [21]. The crystallite sizes associated with (111) peak of CuO were calculated using the Scherrer formula, shown in Eq.1 [21].

$$D = \frac{k\lambda}{\beta \cos\theta} \tag{1}$$

where k, λ, θ, $and\beta$are constants, the wavelength of the X-ray, full width at half maximum, and the Bragg's angle, respectively. As depicted in Table 1, crystallite sizes decrease with an increase in Zn concentration up to 1.0 wt% Zn. At higher concentrations of Zn (i.e., 2 wt%), the crystallite size increased, Table 1.

. While the lattice strain, which was computed using Eq. 2 [21] increases with an increase in Zn concentration up to 1.0 wt%. While at 2 wt% Zn, the lattice strain decreased.

$$\varepsilon = \frac{\beta \cos\theta}{4} \tag{2}$$

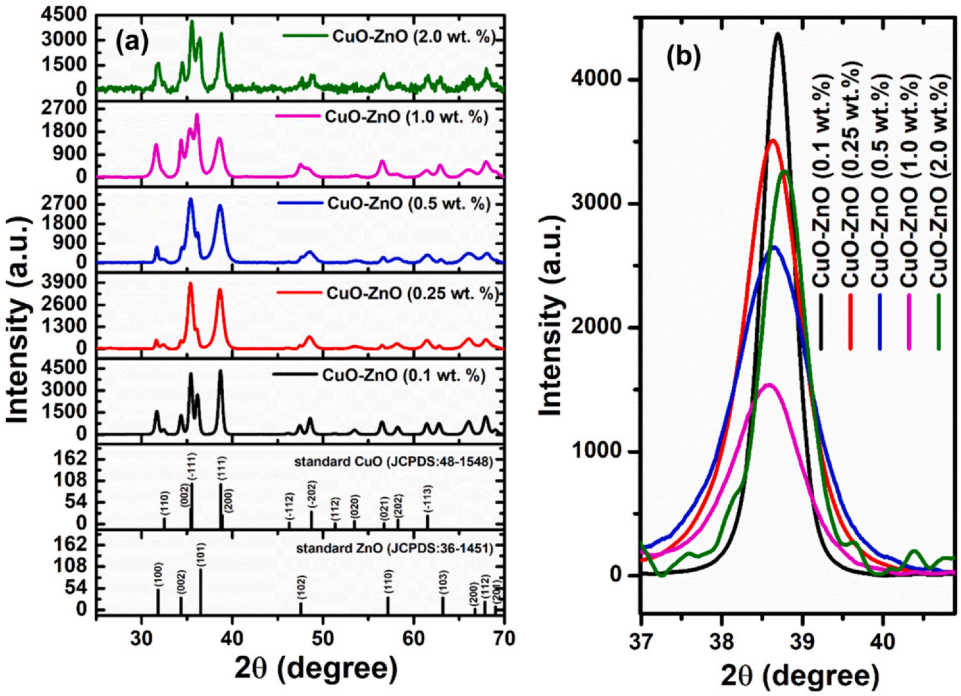

Fig. 1. XRD patterns of CuO-ZnO heterostructures prepared by varying Zn wt%, (b) crystallite sizes versus the Zn wt%, (b) Magnified CuO (111) peak for the CuO-ZnO heterostructures.

Table1
Calculation of crystallite size, dislocation density, and strain.

Samples name	Crystal plane (111)		
	Crystallite size (D)	Dislocation density, δ ($\times 10^{-2}$ nm^{-2})	Strain, ε ($\times 10^{-3}$)
CuO-ZnO (0.1 wt%)	17.95	0.310	3.00
CuO-ZnO (0.25 wt%)	9.9	1.00	3.50
CuO-ZnO (0.5 wt%)	8.45	1.40	4.10
CuO-ZnO (1.0 wt%)	7.7	1.70	4.50
CuO-ZnO (2.0 wt%)	13.42	0.50	2.60

The quantity of crystal defects, or the irregularity, which exists within a crystal structure, was utilized to calculate the dislocation density. A dislocation is a certain type of topological imperfection existing in the material. The dislocation density was computed using the formula shown in Eq. 3 [21]:

$$\delta = \frac{1}{D^2} \tag{3}$$

As listed in Table 1, the dislocation density increases with an increase in Zn concentration (i.e., up to 1.0 wt%) in the CuO matrix. While at 2.0 wt%, the dislocation density decreased. Thus, it can be anticipated that the CuO-ZnO (1.0 wt%), which has the minimal crystallite size, the highest strain, and dislocation density could lead to superior sensor sensitivity towards gas adsorption. Since larger dislocation density and strain result in improved surface defects, thus this leads to higher gas molecules adsorption on the sensor surface, hence improving the sensor response [22,23].

Fig. 2 depicts the SEM analyses of CuO-ZnO heterostructures with different concentrations of Zn (0.1–1 wt%). At lower Zn incorporation on CuO matrix, i.e., 0.1–0.25 wt% (Fig. 2**(a-d)**), larger sharp nano-needles/spear structures with an estimated average thickness of 28 nm associated with ZnO were observed, see the low resolution (LR) image in Fig. 2**(a and c)**. Thus, in LR and high-resolution (HR) images in Fig. 2**(a and b)**, flower-like structures are surrounded by larger sharp nano-needles/spear structures. This was validated by the higher XRD peaks intensity detected at low ZnO concentrations, justifying the unregularly formation of ZnO at low concentrations.

This justifies that the formation of ZnO nuclei at lower concentrations was quicker than that of CuO. Nonetheless, when increasing the ZnO concentration, Fig. 2**(c)**, the nanorods stacked on top of nanoplatelets with a projected average diameter of 1.0 µm are observed. At 0.5 wt% (Fig. 2**e and f**), the nanorods surrounded by smaller nanoplatelets are observed. At higher Zn concentration (i.e., CuO-ZnO (1.0 wt%), Fig. 2**(g and h)**, the cluster of "nano-crumbs-like" structures arranged in a scattered form. Moreover, the shape of the "nano-needles/spear-like" structure began to fade and cracks with rough wrinkles began to appear with a rough surface. While the CuO-ZnO (2 wt%) shows a platelets-like structure surrounded by spherical structures, see Fig. S1. Therefore, the variation in weight ratio had indeed an effect on the structure and morphologies of the material.

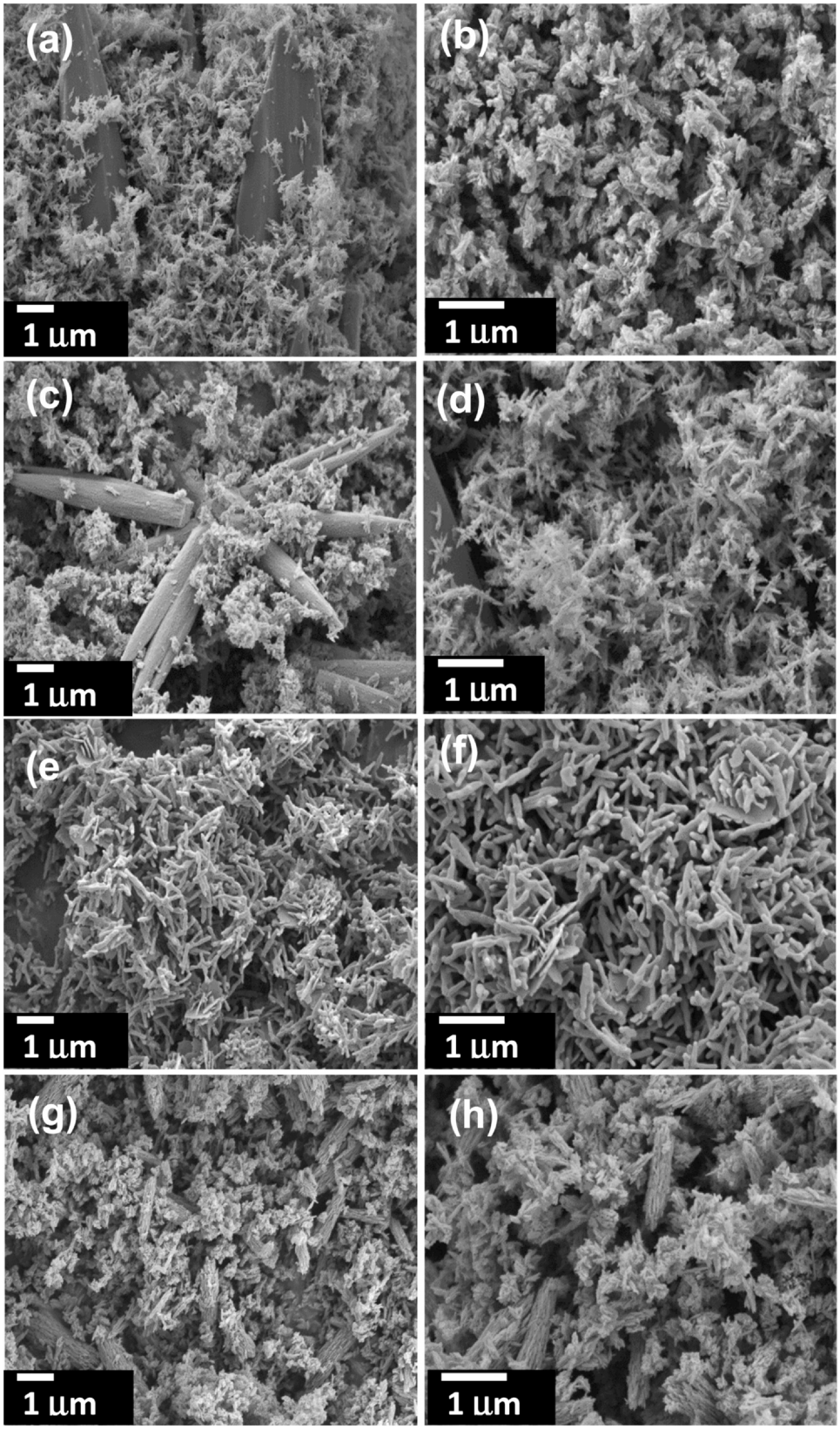

Fig. 2. LR- and HR-SEM images of (a-b) CuO-ZnO (0.1 wt%), (c-d) CuO-ZnO (0.25 wt%), (e-f) CuO-ZnO (0.5 wt%), (g-h) CuO-ZnO (1.0 wt%).

TEM analyses were further carried out to probe the internal structure of the heterostructures. Fig. 3**(a and b)** illustrates the low- and high-resolution TEM micrographs and the SAED patterns (Fig. 3**(c))** of the p-n CuO-ZnO (1.0 wt%) heterostructures. The low resolution (LR)-TEM analyses in Fig. 3**a** and Fig. S2 show rod-like structures. While the higher resolution (HR) in Fig. 3**(b)** shows lattice fringes of 0.208 nm corresponding to (111) lattice plane of CuO. Additionally, the lattice spacing of 0.247 nm associated with ZnO was

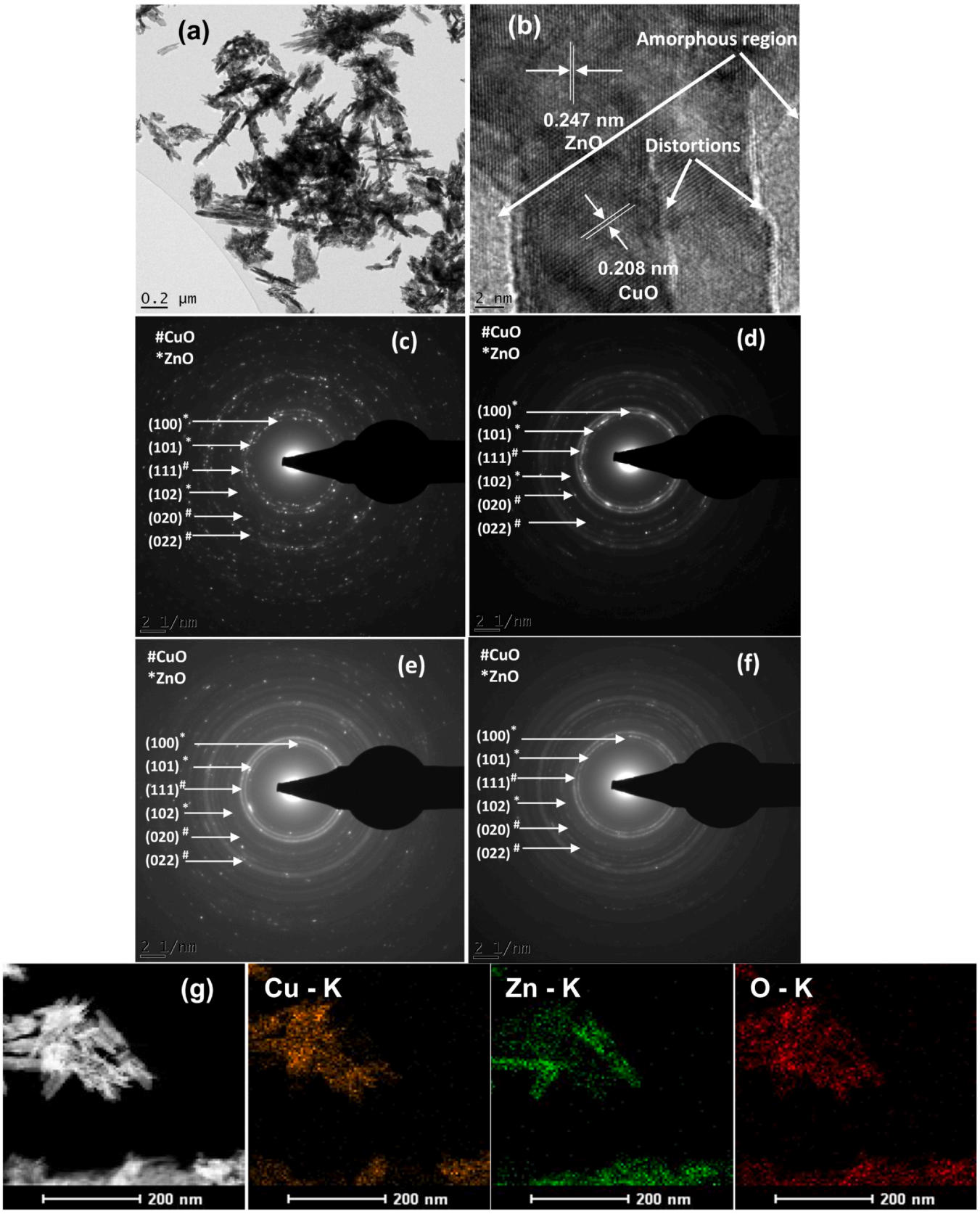

Fig. 3. (a, b) LR and HR-TEM of CuO-ZnO (1.0 wt%). Note that (c-f) corresponds to SAED patterns of (c) CuO-ZnO (0.1 wt%), (d) CuO-ZnO (0.25 wt%), (e) CuO-ZnO (0.5 wt%), (f) CuO-ZnO (1.0 wt%). (g) STEM-EDS maps of CuO-ZnO (1.0 wt%).

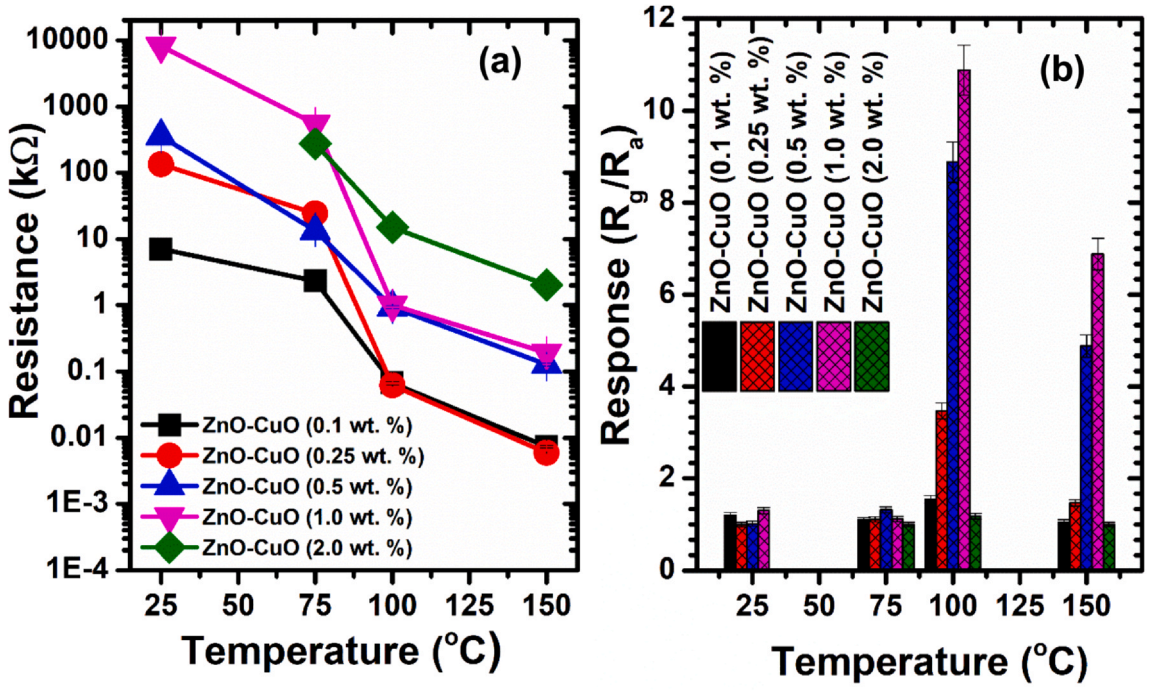

Fig. 4. R_a versus the operational temperature, (a) the response of various sensors towards 100 ppm xylene vapour versus the operational temperature.

also observed. As presented in Fig. 3**(b)**, the incorporation of Zn into the CuO lattice produced strain in the system that is released by generating lattice distortions, such as stacking faults in the crystal planes [24]. SAED patterns in Fig. 3**(c-f)** show that the materials are polycrystalline. The (100), (002), (102), (111), (020), and (022) planes shown from the SAED patterns correspond to ZnO and CuO structures, respectively. These findings are in-line with the XRD results. Furthermore, the diffused diffraction patterns are observed from the SAED patterns when increasing the doping concentration of Zn in the CuO lattice (see Fig. 3**(c-f)).** This behaviour is consistent with the XRD analyses. STEM- EDS SI maps in Fig. 3**(g)** and Fig. S3 show different colour maps of the CuO-ZnO (0.1–0.5 wt%), which displays the elemental composition of the individual heterojunctions and confirm the dual composition of each nanostructure. This confirms a uniform distribution of Zn in the CuO matrix, which led to the formation of CuO-ZnO heterostructures. However, the maps of the CuO-ZnO (2.0 wt%), (Fig. S4) clearly show an inhomogeneous distribution of Zn in the CuO matrix, where the two materials show a phase separation.

3.1. Gas sensing performance towards Xylene

To regulate an optimal operational temperature, the sensor resistance towards various gases was probed. The sensor resistance of all the sensors shows a clear decrease when increasing the operational temperature, see Fig. 4**(a)**. This behavior is regulated by the intrinsic characteristic of SMO [25]. The plot of the response versus the operational temperature is depicted in Fig. 4**(b)**. Indeed, almost all the sensors show an increase in response to the operational temperature, except the 0.1 wt%, which did show much improvement. Among the sensors, the CuO-ZnO (1.0 wt%) showed a greater response of 10.9 towards 100 ppm of xylene vapour in comparison to other sensors.

The dynamic resistance plots of various sensors towards 5–100 ppm xylene measured at 100 °C are exhibited in Fig. 5**(a)**. The sensors clearly show a continuous change in resistance towards various concentrations of xylene, displaying a continuous response/recovery behaviour. This behaviour is validated by the sensor response plot illustrated in Fig. 5**(b)**, where the sensor response increases with increased xylene concentration. Nonetheless as depicted in Fig. 5**(a)**, all the sensors show some drift with the increase in gas concentration. This drift could be associated with the interaction between the xylene and the surface of the sensor, where the xylene residuals could have stayed on the sensor surface. Additionally, at the low operational temperature of 100 °C, the rate of reaction between the xylene gas and the sensor surface could be too slow to result in a significant change in the sensor recovery rate. Thus, this shows that the steady state has not been realized in the cycles. The drift could probably be improved by either providing more recovery time or perhaps introducing noble metals on the surface of the CuO-ZnO heterostructure to improve the reaction rate [26,27].

The plots of the response versus the xylene concentration depicted in Fig. 5**(c)**, show that the sensor's response indeed increases with the gas concentration (5–100 ppm), where the CuO-ZnO (0.5 wt %) and CuO-ZnO (1.0 wt%) disclosed an exponential growth with increased xylene concentration. Though the CuO-ZnO (1.0 wt %)-based sensor demonstrated improved response in comparison to its counterparts. The sensor disclosed responses of 1.87 and 10.88 at 5 ppm and 100 ppm xylene concentrations, respectively. Nonetheless, for the CuO-ZnO (2.0 wt%), the response reduced drastically. This could be associated with the aggregation between the ZnO and CuO, due to a higher amount of Zn content, which led to a roughening of the grain growth, see (Fig. S4), leading to a lower sensing performance. Kruefu et al. [28] observed that at higher concentrations (1.0 wt%), the nanoparticles of Ru agglomerated into bigger

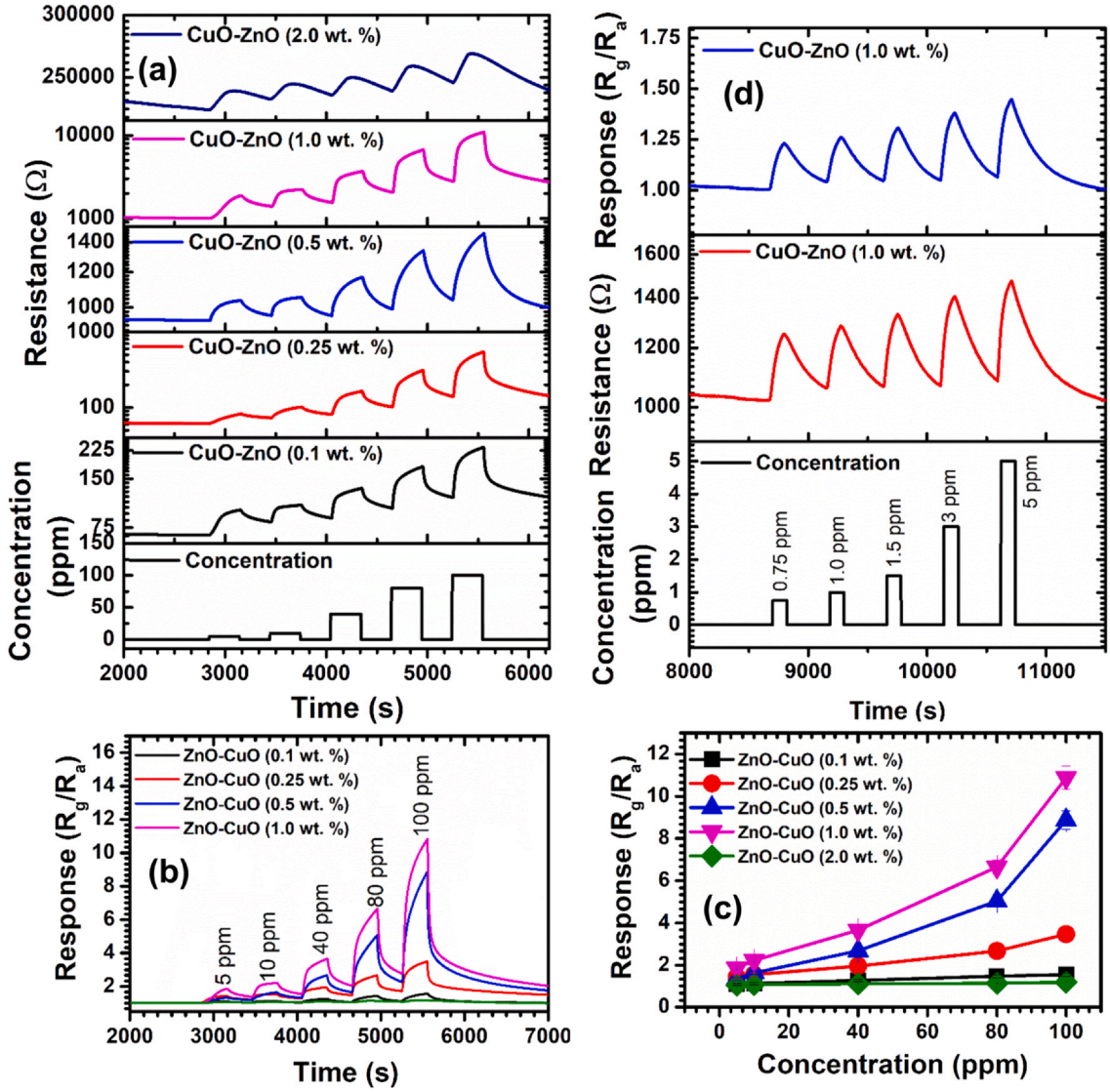

Fig. 5. (a) Dynamic resistance plot, (b) transient response plot, and (c) response against the xylene concentration measured at 100 °C. (d) Dynamic resistance plot at lower xylene concentrations, and response against concentration measured at 100 °C.

nanoparticles, resulting in poorer dispersion, as a result, an inferior sensing response was observed.

Since the current performing sensor (i.e., 1.0 wt%) showed the best response even at a lower concentration of 5 ppm, therefore the change in resistance was further measured at the lowest concentrations (0.75–5 ppm). The sensor still showed a response of 1.23 at the lowest concentration (i.e., 0.75 ppm) our system could measure, Fig. 5**(d)**. The response also increased with xylene concentration.

Fig. 6**(a)** displays the calibration curves (linear fit) of various sensors toward 5–80 ppm xylene vapour at 100 °C. As revealed in Fig. 6**(a)**, the ZnO-CuO (1.0 wt%) heterostructure-based sensor shows higher sensitivity (slope=0.063 ppm^{-1}) towards xylene than other sensors. Moreover, the correlation coefficients (R^2) of roughly 0.98–1 were realized for all the sensors, which confirmed the consistent detection of the sensors towards xylene.

The limit of detection (LoD) is also another vital parameter to show the lowest concentration level, which the sensors can detect the target, more especially in the case of a leak. Thus, the LoD was computed using the following expression: $LoD = 3\left(\frac{RMS_{noise}}{Slope}\right)$, and the $RMS_{noise} = \sqrt{\sum_i (x_i - x)^2/N}$, which is associated with the room-mean-square that is taken from the fluctuation of the sensor resistance prior the introduction of the target gas in the chamber. Note that the x_i and x are the experimental data point, and N is the average of the data points. As a result, from the expression above, the *LoD* of 0.111, 0.039, 0.011, and 0.0095 ppm were realized for the CuO-ZnO (0.1 wt %), CuO-ZnO (0.25 wt%), CuO-ZnO (0.5 wt%), and CuO-ZnO (1.0 wt%), respectively. The minimal *LoD* of 9.5 ppb may be influenced by abundant oxygen vacancy, enhancing the gas sensing capabilities. This indeed confirms that CuO-ZnO (1.0 wt%) sensor can detect an ultra-low xylene vapour of 9.5 ppb, indicating that the CuO-ZnO

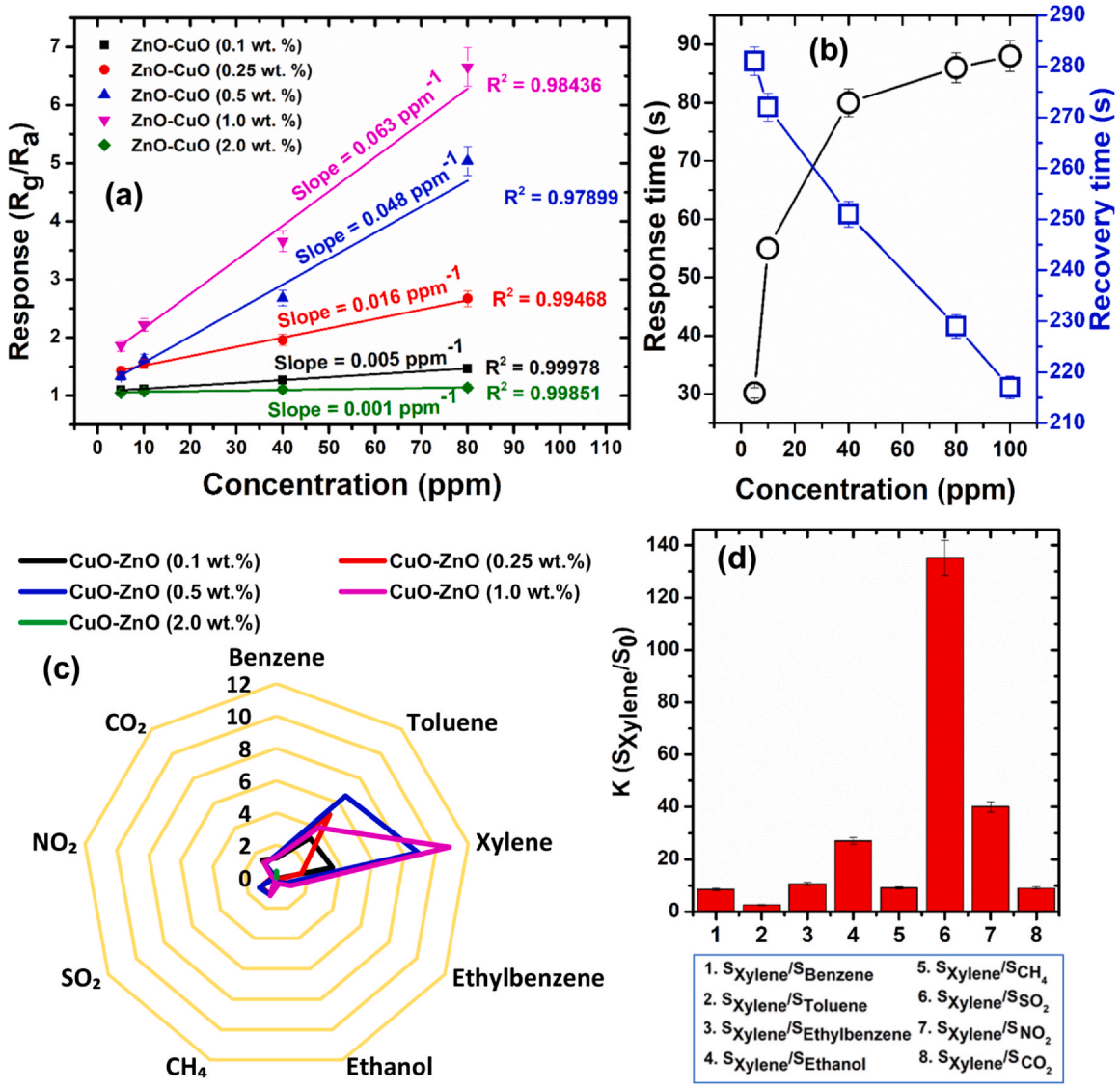

Fig. 6. (a) Calibration curves for the sensitivity and LOD calculations, (b) response /recovery times at various xylene concentrations, (c) The radar graph, and (d) cross-sensitivity plot towards xylene over other interference gases.

(1.0 wt%) heterostructure-based sensor can realize sub-ppb-level concentration.

Another vital parameter of the sensors for real-world application is the response/recovery times. The response/recovery times denote the times the sensor is obligated to fulfil 90% of the resistance variation when exposed to analyte gas and / 10% when recovered in air, respectively. Fig. 6**(b)** shows the plot of the response/recovery times of the CuO-ZnO (1.0 wt%)-based sensor to various xylene concentrations. Though the response time increases with xylene concentration, nonetheless, at 100 ppm, the sensor still revealed a response time of 87 s, while the recovery time was slightly longer (216 s) at 100 ppm. The rapid response can be associated with improved surface defects, which hastens the reaction of xylene and energetic oxygen species.

The capability of SMO-based sensors to classify the target gas within other interference gases is a critical principle to assess the gas sensor performance [29]. As a result, in the current work, the sensors were exposed to different gases at 100 ppm, which included BTX, CH_4, SO_2, NO_2, and CO_2 as shown in the radar plot. It is evident that among the tested sensors, the sensor based on CuO-ZnO (1.0 wt%) heterostructure established a greater response of 10.88 and improved selectivity towards 100 ppm xylene compared to other interference gases. The detected 100 ppm concentration of xylene agrees with the endorsed permissible exposure level set by Occupational Safety and Health Administration (OSHA) for an 8-hour time-weighted average (TWA) concentration [30]. Thus, the selective detection of xylene at 100 ppm illustrates the potential application of the CuO-ZnO (1.0 wt%) heterostructure-based sensor for indoor quality monitoring.

Furthermore, the CuO-ZnO (1.0 wt%) heterostructure-based sensor showed superior selectivity with low cross-sensitivity to interfering gases (see Fig. 6**(c)**), such as benzene ($S_{xylene}/S_{benzene}$= 8.5) and toluene ($S_{xylene}/S_{toluene}$ = 2.7). The current cross-sensitivity value is lower than that reported by Woo et al. [31], which was $S_{xylene}/S_{toluene}$ = 2.3. It is further observed from the Figure that SO_2 has the

most insignificant cross-sensitivity (S_{xylene}/S_{SO2}= 135.25) towards xylene detection. Basically, the cross-sensitivity ratios ranged from 2.7 (toluene) to 135 (SO_2). This served to demonstrate the outstanding selectivity of the sensor that is critical for its discriminability to xylene in real conditions. Though we should point out that the dissimilarity between the alike chemistry of xylene and toluene utilizing SMO-based sensors is reflected as the most challenging issue in the gas sensing fraternity to selectively detect one in the presence of the other.

From this standpoint, the current CuO-ZnO (1.0 wt%) based sensor can be adopted as an excellent device for selective detection of xylene vapour at lower operational temperatures. The current selectivity towards xylene over other interference gases, such as BTE, could be justified based on the following points:

(1) The difference in the number of methyl groups has a significant influence on selectivity. For instance, xylene has one additional methyl group compared to toluene, as a result, it is very reactive with a higher oxidation rate [32,33]. A previous study by Russell's reported a higher oxidation rate of 0.0039 mol h^{-1} for xylene at 90 °C in comparison to 0.0013 mol h^{-1} for toluene [34].
(2) The bond energy of the BTEX also plays vital a role in the gas sensing performance [35]. Generally, bond energies (BE) of toluene and xylene are the lowest and differ slightly, which are respectively 356 and 375 kJ/mol. While both benzene and ethylbenzene have the highest BE of 431 and 435 kJ/mol, respectively [36,37]. Though toluene has the lowest BE, nonetheless it possesses exceptional chemical stability under distinctive conditions and CH_3 is much more stable than OH and CHO. As a result, this makes it difficult to react, though it can react radically with an oxidant or acid.
(3) The other reason could be due to the enthalpy change of the dehydrogenation process [38,39]. For instance, among the BTEX, the enthalpy variation of the dehydrogenation of both toluene and xylene only differs by 0.4 J/mol, which is about 157.8 and 157.4 J/mol for toluene and xylene, respectively [40,41]. Nonetheless, the enthalpy change of benzene is almost higher by a value of 100, than those of toluene and xylene, which is 255.4 kJ/mol.
(4) As shown from the XRD and TEM analyses, the CuO-ZnO (0.1 wt %), CuO-ZnO (0.5 wt%), and CuO-ZnO (1.0 wt%) show higher exposed (100) facets for the ZnO, which showed better selectivity towards xylene. Though, it is observed that for CuO-ZnO (1.0 wt %), the selectivity towards xylene is more improved, due to enhanced exposed (100) facets [42–44]. Nonetheless, more work is needed to verify our assumptions.
(5) The CuO-ZnO (1.0 wt%.), has a higher number of heterojunctions compared to those with lower Zn wt%. More p-n heterojunctions resulted in improved sensing response [45]. Nonetheless, studies have shown that when increasing the doping or loading concentration could result in poor performance. Such decrease could be associated with the percolation influence, where additional p-CuO-n-ZnO homojunctions are developed in the sensing layer, thus reducing the number of p-n heterojunctions that are more active for modulation of the resistance as reported by previous studies [46–48].

Therefore, though toluene showed slightly lower BE and change in enthalpy of dehydrogenation, however, the additional methyl group and higher oxidation rate of xylene justify the higher selectivity of CuO-ZnO (1.0 wt%) heterostructure-based sensor towards xylene vapour. Moreover, as observed from the selectivity plot, the order of response is xylene > toluene > benzene, justify the above observation.

In addition to selectivity, the repeatability, as well as the sensor durability (i.e., long-term stability) are also vital parameters for the practical application and commercialization of SMO-based gas sensors. Fig. 7**(a)** shows the repeatability plot of the CuO-ZnO (1.0 wt%) heterostructure-based sensor tested towards fixed xylene concentration of 100 ppm at 100 °C, showing 8 successive response and recovery cycles. The sensor displays almost identical responses/recovery cycles, confirming its possible usage for the detection of xylene for indoor air quality.

The influence of humidity on the sensor characteristics was then studied. The change in the CuO-ZnO (1.0 wt%) sensor resistance was tested towards five successive cycles of 100 ppm xylene under 10%, 20%, 30%, and 40% RH at 100 °C, see Fig. 7**(b)** and Fig. S5. Indeed, the response was slightly reduced by 27%, 30%, 47%, and 22% in the presence of 10%, 20%, 30%, and 40% RH, respectively (Fig. 7**(c)**). This justifies that RH hampers the adsorption of oxygen and leads to fewer oxygen ions. It is evident that at 40% RH, the response slightly increased in comparison to that of 20% RH. This behavior has also been witnessed by previous researchers [49–51]. This is probably due to that at higher RH conditions, the interaction of the CuO-ZnO-based sensor with xylene is stimulated by humidity. To validate this, the t_{res} and t_{rec} were calculated for dry air and RH analyses, see Fig. S6**.** Remarkably, the t_{res} increases with an increase in RH, while the t_{rec} decreases, denoting that humidity acts as a catalyst towards t_{rec}. In dry conditions, the t_{rec} of the CuO-ZnO is higher compared to that of RH conditions. Thus, the contribution of RH improved the interaction between n-type metal oxide surface and atmospheric oxygen and thus acts as a catalyst for xylene gas. This behavior was previously reported by Tshabalala et al. [50], where they observed a decrease in t_{res} and t_{rec} with an increase in RH conditions. Nonetheless, more work is required to clearly understand the role of RH in the reduced t_{rec}.

Long-term stability is also another vital parameter required for real-time application. Thus, the stability of the CuO-ZnO (1.0 wt%) heterostructure-based sensor towards xylene vapour was tested for a period of 30 days in dry air and under the existence of 40% RH, see Fig. 7**(d)**. It is evident that the response of the sensor towards xylene only reduced by 4.8% and 6.3% in dry and 40% RH. This trivial variation indeed shows that the CuO-ZnO (1.0 wt%) heterostructure-based sensor possesses good long-term stability detection of xylene and can be utilized for real-time application.

Table 2 compares the xylene sensing characteristics of the current work and that of other published studies. Most of the fabricated sensors were achieved using the hydrothermal approach, due to its exceptional advantages such as low synthesis temperature and providing large production of nanomaterials. As observed in Table 2, the current sensor displays a lower operational temperature of 100 °C, in comparison to the published studies, indicating the benefit of low power consumption. Moreover, the low operational temperature could reduce the crystal growth and prolong the sensor lifetime and benefit the practical application. Certainly, our current sensor also shows a better response time than NiO/$NiCr_2O_4$ [53], Sn-NiO, [54] and SnO_2-Co_3O_4 [55].

3.2. Xylene Gas Sensing Mechanism

Currently, the mechanism of gas sensing for SMO is built on the variation of sensor resistance due to the adsorption/desorption process. Since p-n CuO-ZnO heterostructure-based sensor acts as a p-type semiconductor, thus, the holes are the major carriers. When

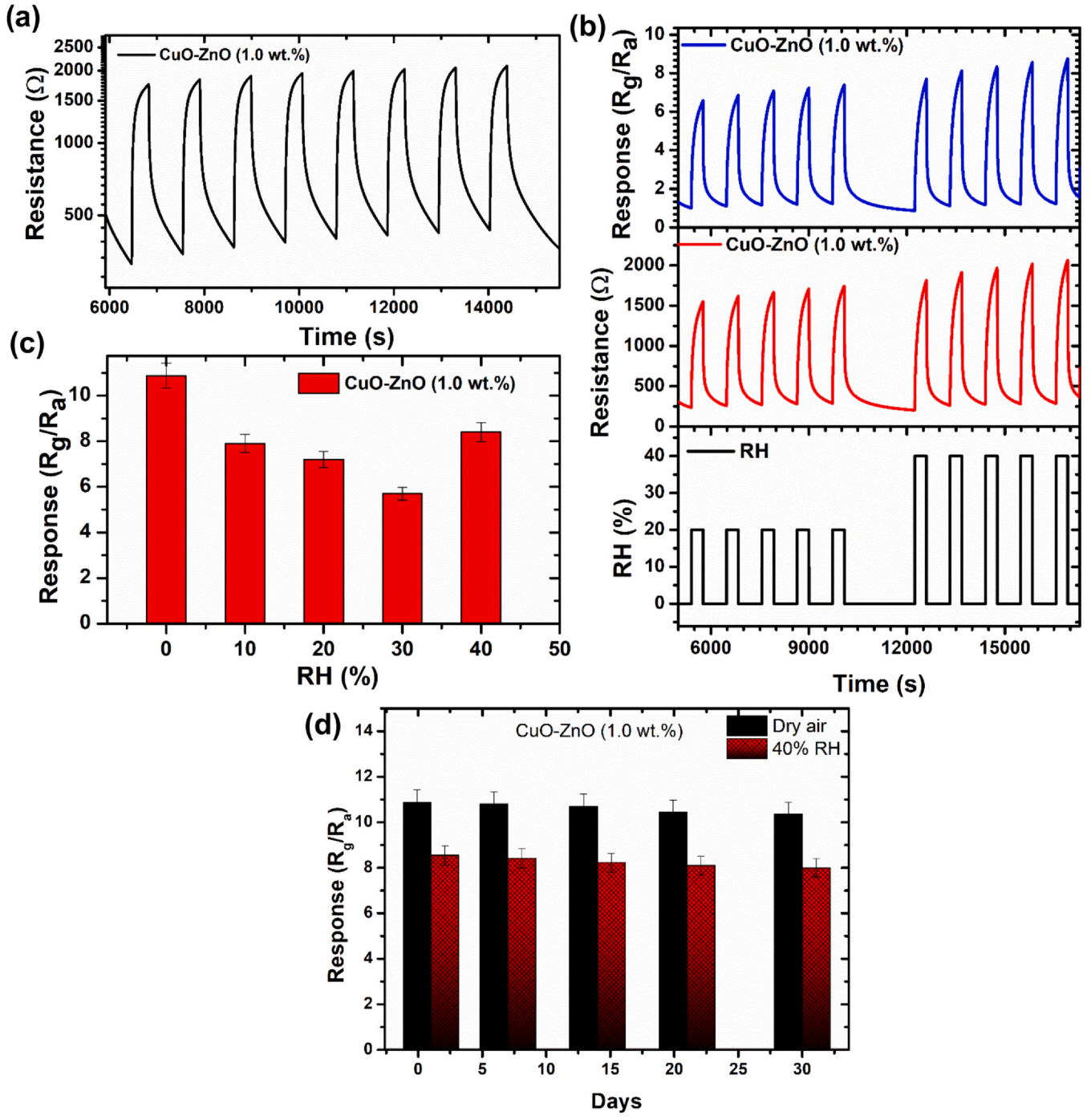

Fig. 7. (a) Repeatability, (b) Resistance and response plots at various RH percentages, (c) Response against RH (%), and (d) A plot displaying long-term stability results in dry air and 40% RH. Note all the measurements in this Figure were done at 100 °C.

exposing the CuO-ZnO heterostructure-based sensor to air at an operational temperature of 100 °C, oxygen molecules are adsorbed on the sensor surface, hence creating adsorbed oxygen anion species (O^-),see Scheme 1**(a)** and reaction (1, 2) by interacting with free electrons (e^-)from conductance. As a result, the charge carriers increase, leading to the creation of a thick hole accumulation layer (HAL) [56–63].

$$O_{2(gas)} \rightarrow O_{2(ads)} \quad (4)$$

$$O_2(gas) + e^- \rightarrow 2O^-(ads)(100\ \ ^oC < 300\ \ ^oC) \quad (5)$$

However, once the CuO-ZnO (1.0 wt%) is tested towards analyte gas, like xylene, xylene vapour, it would interact with the adsorbed oxygen anion species (O^-), leading to the release of the electrons of

Table 2
Summary of published work on xylene sensor compared to the current work.

Sensing element	Method	Conc. (ppm)	T_{res}/T_{rec} (s)	Response	Temp. (°C)	LOD (ppm)	Refs.
CuO-ZnO	Hydrothermal	100	87/216	10.88	100	0.0095	This work
Pt- Cr_2O_3-WO_3	Hydrothermal	10	5/736	75.3	225	0.50	[49]
TiO_2-Nanowires	Hydrothermal	100	45/95	37	125	0.937	[50]
Sn-SnO_2 nanocomposite	solvothermal method	100	1.5/40	3.13	25	1.9	[51]
SnO_2/Co_3O_4	Hydrothermal	100	98/107	47.8	280	-	[52]
NiO/$NiCr_2O_4$	Hydrothermal	100	1217/597	66.2	225	0.05	[53]
Sn-NiO	Hydrothermal	100	298/223	20.2	225	0.30	[54]
SnO_2- Co_3O_4	Hydrothermal	100	204/367	101	175	0.05	[55]

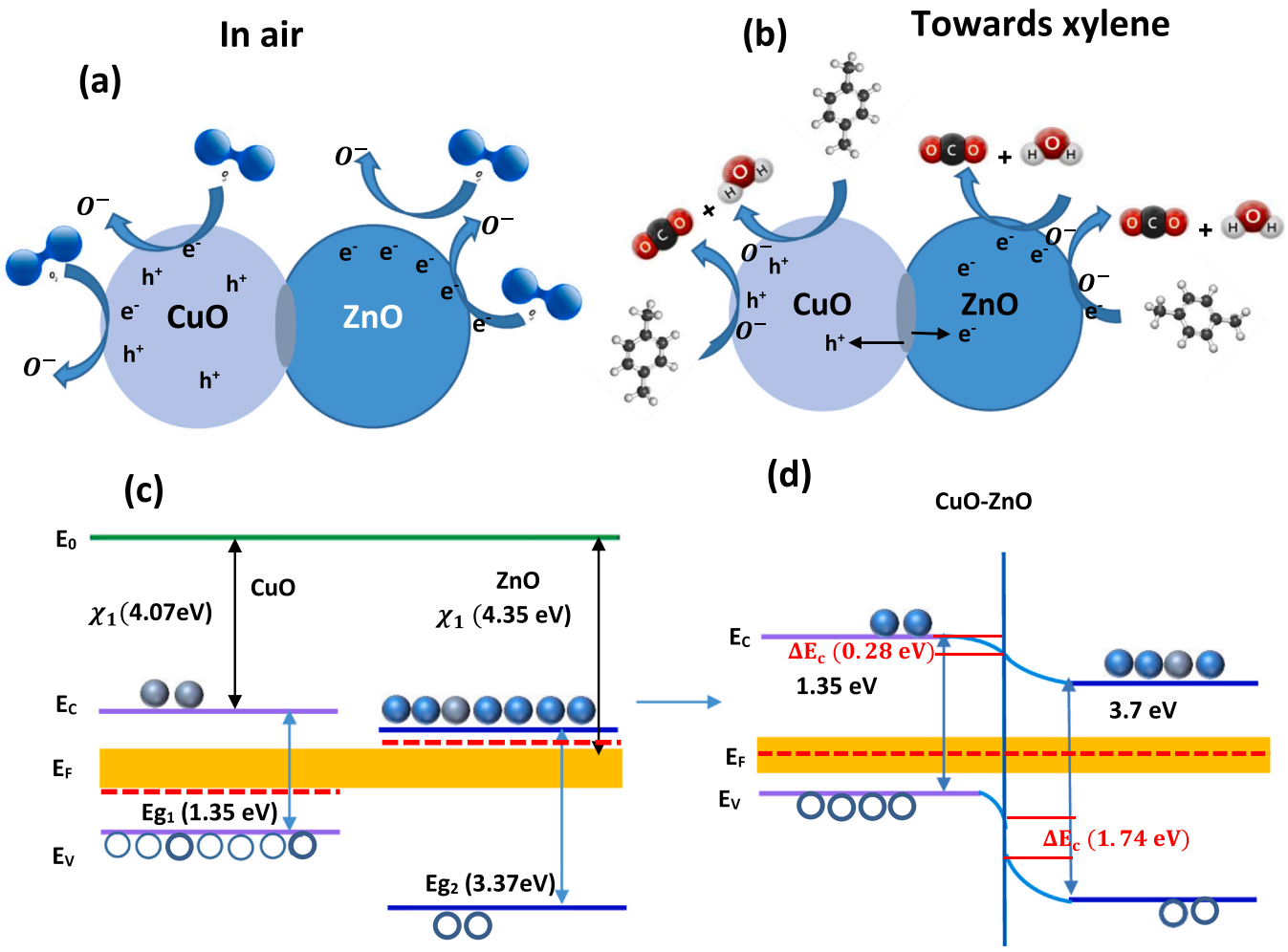

Scheme 1. Sensing mechanism of CuO-ZnO (1.0 wt%)-based sensor (a) in air and (b) towards xylene vapour at 100 °C, (c-d) energy band diagram in air and towards xylene vapour.

the captured into the material. The free electrons will consume the holes in CuO and result in surplus electrons in ZnO, as a result, the depletion layer width will reduce. Owing to the formed p-n nano-junctions, the holes that are consumed in CuO would hastily be added from the electron depletion layer at p-n junctions. Then, the holes in the CuO-ZnO heterojunction will move to CuO across the interface and the electrons migrate to the conduction band, leading to an increase in the charge carrier concentration, resulting in a reduced resistivity. Therefore, the CO_2, H_2O, and electrons will be released as shown in Scheme 1**(b)** and reaction (2) [50–53].

$$(C_6H_4CH_3CH_3)_{gas} \leftrightarrow (C_6H_4CH_3CH_3)_{ads} \quad (6)$$

$$(C_6H_4CH_3CH_3)_{ads} + 21O^- \rightarrow 8CO_2 + 5H_2O + 21e^- \quad (7)$$

While the superior selectivity was justified above, thus the improved sensitivity of CuO-ZnO (1.0 wt%) compared to other sensors could be justified by the formation of a depletion layer induced by the adsorption of the oxygen species at the interface of p-n heterojunction between the CuO and ZnO surface as depicted in Scheme 1**(c)**. In general oxygen deficiency of ZnO displays an n-type, while

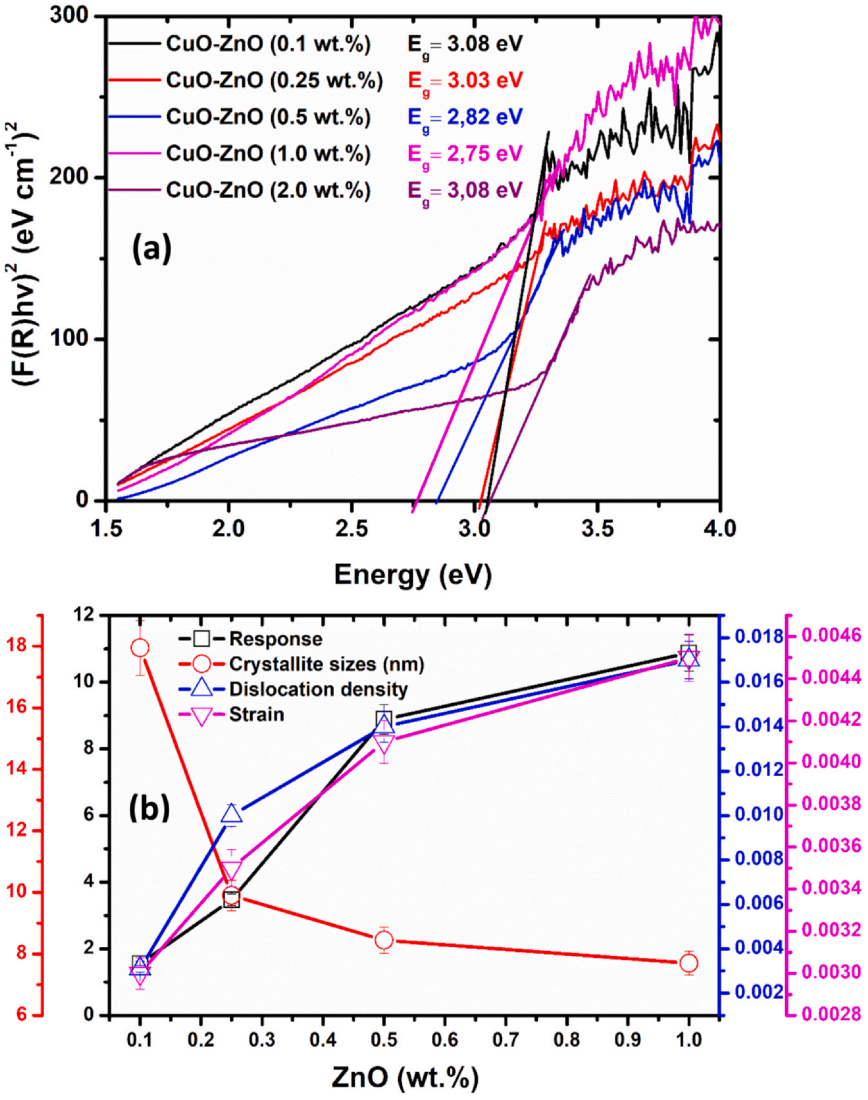

Fig. 8. **(a)** Kubelka–Munk function figure utilized for estimation of the band gap, **(b)** Relationship between the response, crystallite size and dislocation, density, and strain of CuO-ZnO at various Zn concentrations.

an oxygen excess CuO displays a p-type conductivity. Generally, ZnO contains a higher bandgap (3.4 eV), as well as a higher electron affinity of 4.35 eV compared to CuO (1.35 eV) and 4.07 eV. Thus, the difference in a Fermi level shown in Scheme 1**(c)**, will lead to the electron's movement from the conduction band of ZnO to CuO, whereas holes will move from the valence band of CuO to ZnO, leading to the formation of a heterojunction (Scheme 1**d**). Thus, the existence of a number of p–n nanojunctions at the interface of CuO and ZnO leads to an extraordinary increase in the heterostructure resistance in comparison to pure ZnO or CuO.

To further justify the superior sensing performance of CuO-ZnO (1.0 wt%) heterostructure, UV/vis measurements of the various CuO-ZnO nanostructures, prepared using various concentrations of ZnO were conducted, as shown in Fig. 8**(a)**. The bandgaps of the CuO-ZnO (0.1 wt%), CuO-ZnO, (0.25 wt%), CuO-ZnO (0,.5 wt%) and CuO-ZnO (1.0 wt%) and CuO-ZnO (2.0 wt%) were estimated on the reflectance data using Kubelka–Munk illustration as 3.08, 3.03, 2.82, 2.75, and 3.08 eV, respectively. Indeed, the CuO-ZnO (1.0 wt%), displayed the lowest bandgap in comparison to other materials. This behavior is consistent with the XRD and TEM analyses, which showed a crystalline behavior of the CuO reducing with increasing the Zn concentration, leading to a defused Debye on the SAED patterns and distortion or reduced (111) plane of the CuO for the CuO-ZnO (1.0 wt %). Generally, the smaller bandgap of CuO-ZnO (1.0 wt%) points out that electrons can be more prone to transition and can produce more photogenerated carriers, which will result in an improved change in sensor resistance and reduced operational temperature. Thus, this justifies the higher sensing performance of the CuO-ZnO (1.0 wt%) heterostructure-based sensor.

To further explore the relationship between the microstructure and the sensing parameters, the behaviour of the maximum response versus crystallite sizes, dislocation density, and strain is shown in Fig. 8**(b)**. Remarkably, the response increases with an increase in strain and dislocation density, while the crystallite sizes decrease, showing a maximum response of 10.88 for the CuO-ZnO (1.0 wt%) heterostructure. Therefore, the addition of Zn in CuO-ZnO

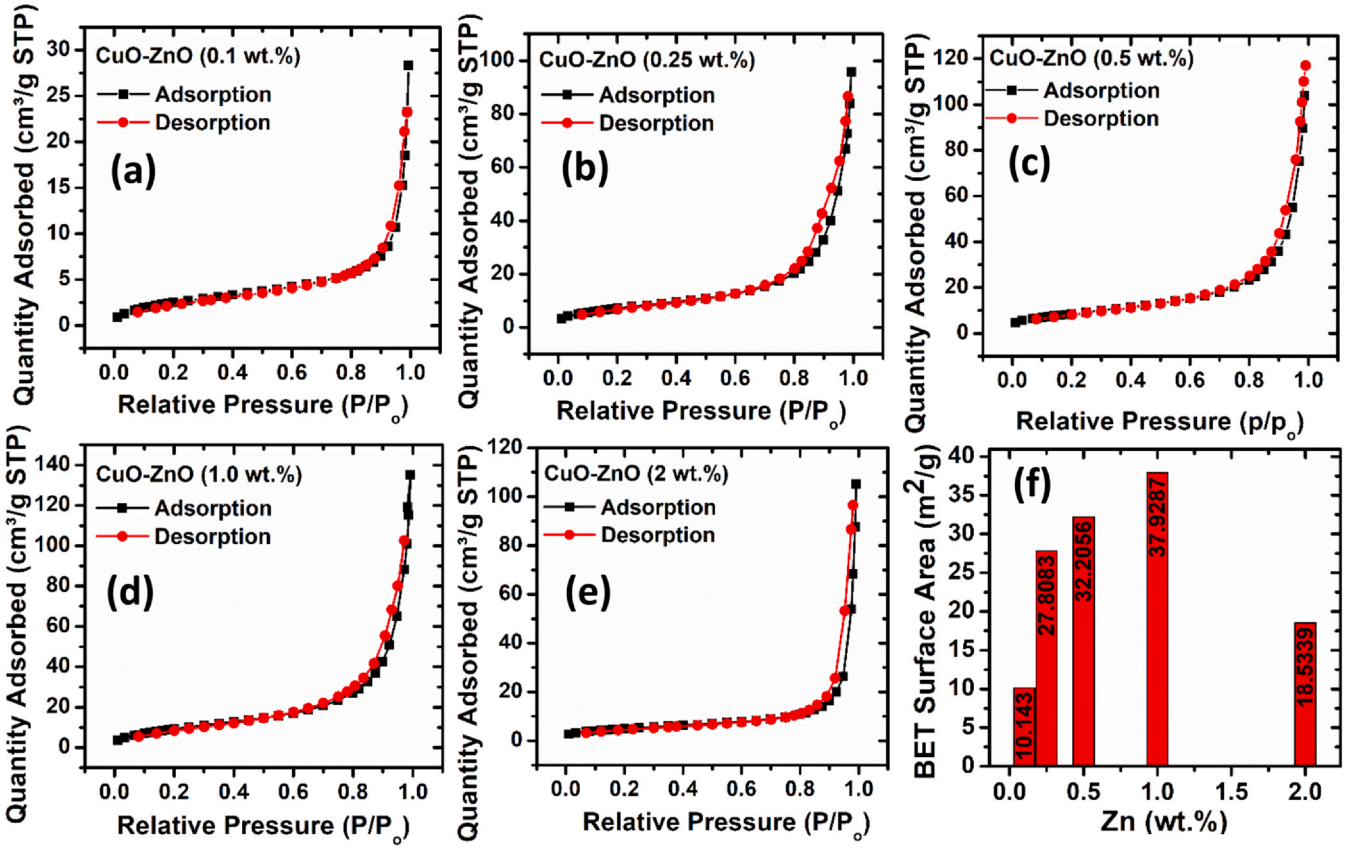

Fig. 9. N_2 adsorbed/desorbed isotherms of the (a) CuO-ZnO (0.1 wt%), (b) CuO-ZnO (0.25 wt%), (c) CuO-ZnO (0.5 wt%), (d) CuO-ZnO (1.0 wt%), (e) CuO-ZnO (2.0 wt%), and (f) BET surface versus Zn concentration.

has a substantial effect on the dislocation density, lattice strain, and crystallite size, which leads to superior performance on the sensing characteristics of CuO-ZnO (1.0 wt%) heterostructure-based sensor.

The BET surface area analyses were carried out to validate the observed sensing performance of the CuO-ZnO heterostructures. Fig. 9 illustrates distinctive nitrogen adsorption/ desorption isotherms for various CuO-ZnO heterostructures. From the plots, the CuO-ZnO (1. wt%) disclosed a higher ability for nitrogen adsorption and desorption in comparison to other nanomaterials. Moreover, the CuO-ZnO (1. wt%) disclosed a superior surface area of 37.9287 m^2/g compared to its counterparts, which justifies improved sensing performance, see Fig. 9**(f)**. This superior surface area is associated with smaller crystalline size observed for the CuO-ZnO (1. wt%) heterostructure, whereas the reduced surface area for the CuO-ZnO (2.0 wt%) could be associated with the agglomerated Zn particles induced by higher incorporation of 2.0 wt% Zn in CuO.

Furthermore, it is extensively acknowledged that the mechanism of gas sensing is associated with the redox reaction between the adsorbed oxygen species and the analyte gas. Therefore, we performed XPS analyses on the CuO-ZnO (1.0 wt%) heterostructure, including its counterparts' materials. The survey spectra of CuO-ZnO heterostructures shown in Fig. S7**(a)** confirm the existence of Cu, O, Zn, and C elements. Fig. 10 demonstrates the high resolution of Cu2p, which illustrates the binding energies of Cu $2p_{1/2}$ and Cu $2p_{3/2}$ at 953.4 eV and 933.4 eV respectively, which are comparable to the typical peaks of Cu^{2+} and established the presence of CuO [64,65]. Clearly, the incorporation of Zn did not much alter the peaks of CuO, instead, the CuO-ZnO heterostructure formed as validated by the Zn2p peaks of ZnO on the supporting information, Fig. S7**(b)**.

Generally, the asymmetric O 1 s peaks may be assigned to three distinctive peaks, such as lattice oxygen (O_L), O^{2-} in CuO or ZnO, oxygen vacancies (V_O), and chemisorbed oxygen species (O_C), which correspond to binding energies of 529.9 eV, 530.5 eV, 531.8 eV, and 532 eV, respectively [65–68]. As depicted in Fig. 10, all the samples could only be fitted into three peaks, centered at 530.8, 531.7, and 532.9 533.3 eV, which could be due to the degree of lattice mismatch at the CuO and ZnO interface [69], leading to increased V_O. The degree of lattice mismatch regulates the V_O content. In Table S1, the V_O concentration in the CuO-ZnO (1.0 wt%) heterostructure was as high as 65.2%, indicating more adsorbed oxygen species participate in the gas sensing reaction. This correlates well with XRD findings. Generally, the V_O content is valuable to yield additional energetic surface sites and creates extra negatively charge oxygen species on the surface that are valuable for enhanced sensing properties. Nonetheless, the O_L are considered as low-active oxygen species that do not play any role in gas sensing reactions, hence poor sensing performance is observed for samples with higher amounts of O_L. Whereas the O_C are strongly and vigorously involved in the redox reactions with the gas molecule adsorbed on the sensing materials. These findings coincided well with the gas sensing characteristics and established the viability of fabricating CuO-ZnO (1.0 wt%), heterostructure to realize admirable gas sensing performance as further observed in Fig. S8, demonstrating a clear correlation between the gas sensing and V_O/O_L ratio.

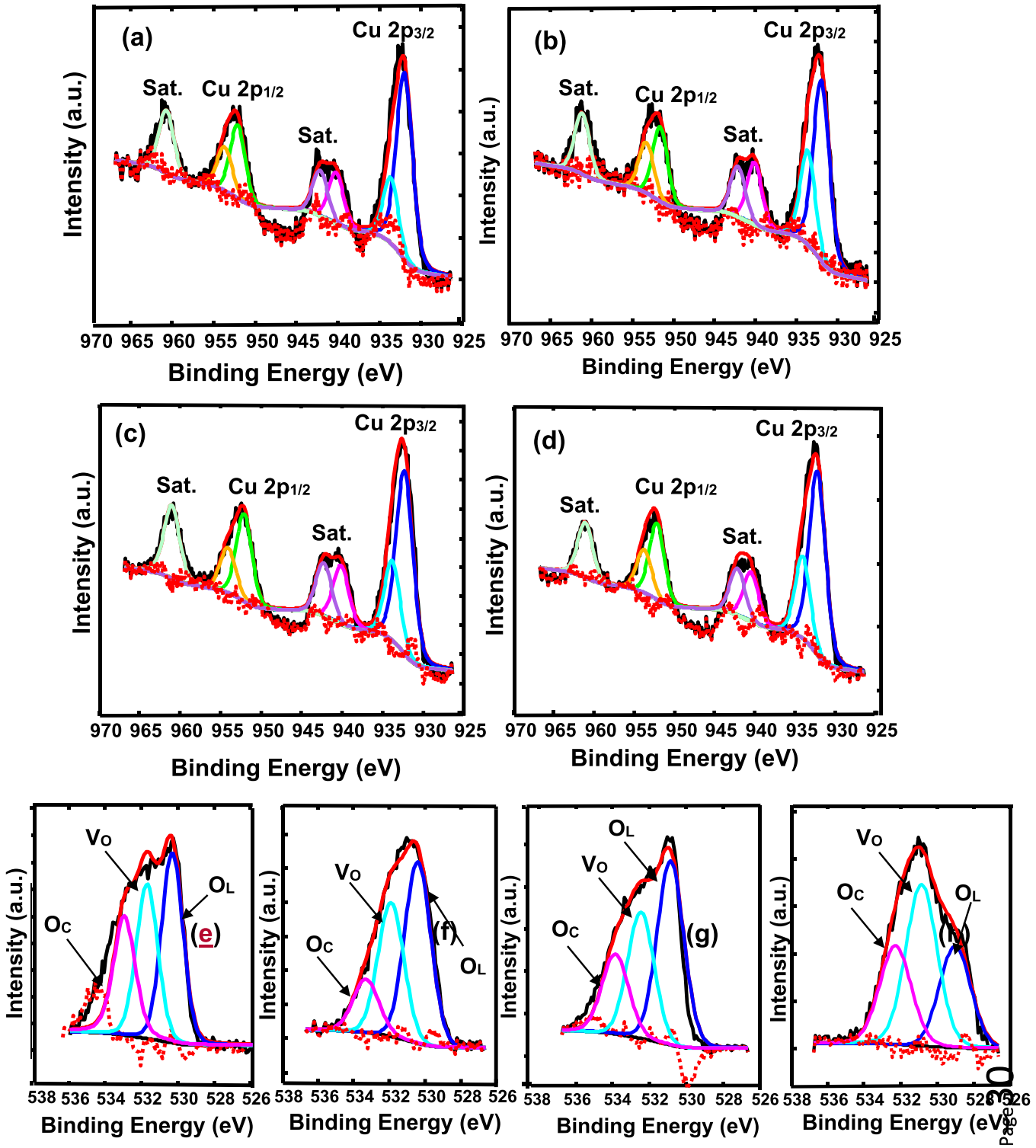

Fig. 10. Cu2p XPS spectra of (a) CuO-ZnO (0.1 wt%), b) CuO-ZnO (0.25 wt%), (c) CuO-ZnO (0.5 wt%), (d) CuO-ZnO(1.0 wt%). O 1 s XPS spectra of (e) CuO-ZnO (0.1 wt%), (f) CuO-ZnO (0.25 wt%), (g) CuO-ZnO (0.5 wt%), (h) CuO-ZnO (1.0 wt%).

4. Conclusion and remarks

In summary, the xylene sensor was successfully fabricated with CuO-ZnO heterostructures as sensing materials. The CuO-ZnO (1.0 wt %)-based sensor demonstrated superior selectivity towards 100 ppm of xylene at 100 °C. Furthermore, insignificant cross-sensitivity towards toluene, benzene, and other interference gases was witnessed. An ultra-low LOD of 9.5 ppb and higher sensitivity of 0.063 ppm^{-1} were observed towards xylene vapour, which showed that the CuO-ZnO (1.0 wt%) heterostructure-based sensor can achieve sub-ppb-level xylene concentration, which basically shows extended detection range of 9.5 ppb-100 ppm. The improved performance of the sensor to xylene can be linked to:

(1) The addition of Zn in CuO-ZnO heterostructure, which had a significant influence on the dislocation density, lattice strain, as

well as on crystallite size, resulted in improved surface defects (i.e., V_O). Therefore, superior sensing performance of CuO-ZnO (1.0 wt%) heterostructure-based sensor could be anticipated.
(2) The reduced band gap provides more xylene adsorption sites and making it easier for xylene to capture electrons in the conduction band.
(3) Superior surface area, which led to improved xylene adsorption on the surface of CuO-ZnO (1.0 wt%) heterostructure-based sensor.
(4) Higher number of heterojunctions for the CuO-ZnO (1.0 wt%.), compared to those with lower Zn wt%. led to more p-n heterojunctions, and as a result, an enhanced sensing response was observed.
(5) The robust chemical affinity and catalytic performance of p-type CuO on xylene vapour.

Moreover, the long-term stability test disclosed that the CuO-ZnO (1.0 wt%) sensor is very stable towards 100 ppm xylene in dry and under 40% RH. Thus, this approach offers an active way for fabricating highly sensitive and selective xylene based derived from CuO-ZnO (1.0 wt%) heterostructure-based sensor for indoor xylene detection.

CRediT authorship contribution statement

Mr. L.M. Maebana: Methodology, Investigation, Software, Writing – original draft, Writing – review & editing. **Dr. R.G. Motsoeneng**: Methodology, Investigation, Software, Writing – review & editing. **Dr. Zamaswazi Tshabalala:** Methodology, Investigation, Software, Writing – review & editing. **Prof. F.R. Cummings**: Software, Writing – review & editing. **Mrs. M. Jozela:** Resources, Writing – review & editing. **Dr. S.S. Nkosi** Investigation, Software, Writing – review & editing. **Prof. H.C. Swart**: Investigation, Writing – review & editing, Resources, Funding acquisition. **Prof. D.E. Motaung:** Conceptualization, Writing – review & editing, Visualization, Project administration, Supervision, Funding acquisition.

Data Availability

Data will be made available on request.

Declaration of Competing Interest

The authors declare that they have no known competing financial interests or personal relationships that could have appeared to influence the work reported in this paper.

Acknowledgements

The National Research Foundation and the Sarchi chair initiative of the Department of Science and Technology (84415) are acknowledged for equipment and financial support.

Appendix A. Supporting information

Supplementary data associated with this article can be found in the online version at doi:10.1016/j.jallcom.2023.170683.

References

[1] WHO, Household Air Pollution and Health, 2018 (accessed on the 18th of July 2022).
[2] E.M. Alsbou, K.W. Omari, BTEX indoor air characteristic values in rural areas of Jordan: Heaters and health risk assessment consequences in winter season, Environ. Pollut. 267 (2020) 115464, https://doi.org/10.1016/j.envpol.2020.115464
[3] E. Gallego, X. Roca, J.F. Perales, X. Guardino, Determining indoor air quality and identifying the origin of odour episodes in indoor environments, J. Environ. Sci. 21 (2009) 333–339, https://doi.org/10.1016/S1001-0742(08)62273-1
[4] J. Wu, G. Yue, W. Chen, Z. Xing, J. Wang, W.R. Wong, Z. Cheng, S.Y. Set, G.S. Murugan, X. Wang, T. Liu, On-chip optical gas sensors based on group-IV materials, ACS Photonics 7 (2020) 2923–2940, https://doi.org/10.1021/acsphotonics.0c00976
[5] G. Yurko, J. Roostaei, T. Dittrich, L. Xu, M. Ewing, Y. Zhang, G. Shreve, Realtime sensor response characteristics of 3 commercial metal oxide sensors for detection of BTEX and chlorinated aliphatic hydrocarbon organic vapors, Chemosensors 7 (2019) 40, https://doi.org/10.3390/chemosensors7030040
[6] R. Nasreddine, V. Person, C.A. Serra, S. Le Calve, Development of a novel portable miniaturized GC for near real-time low level detection of BTEX, Sens. Actuator B Chem. 224 (2016) 159–169, https://doi.org/10.1016/j.snb.2015.09.077
[7] P. Qin, B.A. Day, S. Okur, C. Li, A. Chandresh, C.E. Wilmer, L. Heinke, VOC mixture sensing with a MOF film sensor array: detection and discrimination of Xylene isomers and their ternary blends, ACS Sens 7 (2022) 1666–1675, https://doi.org/10.1021/acssensors.2c00301
[8] J.S. Liu, N. Wang, X.-F. Zhang, Z.-P. Deng, Y.-M. Xu, L.-H. Huo, S. Gao, Facile tree leaf-templated synthesis of mesoporous CeO_2 nanosheets for enhanced sensing detection of p-xylene vapors, J. Alloy. Compd. 889 (2021) 161735, https://doi.org/10.1016/j.jallcom.2021.161735
[9] H. Yang, M.-M. Zhao, L. Li, L.X. Zhang, ZnO nanorods with doubly positive oxygen vacancies for efficient Xylene sensing, ACS Appl. Nano Mater. 5 (2022) 3512–3520, https://doi.org/10.1021/acsanm.1c04146
[10] A. Mirzaei, J.-H. Kim, H.W. Kim, S.S. Kim, Resistive-based gas sensors for detection of benzene, toluene and xylene (BTX) gases: a review, J. Mater. Chem. C. 6 (2018) 4342–4370, https://doi.org/10.1039/C8TC00245B
[11] W. Xu, M. Li, R. Jiang, L. Zhang, M. Du, S. Wang, J. Cao, Facile synthesis of discus-like porous CuO architectures and their enhanced xylene gas sensing performances, Mater. Lett. 324 (2022) 132657, https://doi.org/10.1016/j.matlet.2022.132657
[12] C. Wang, S. Zhang, L. Qiu, S.A. Rasaki, F. Qu, T. Thomas, Y. Liu, M. Yang, Ru-decorated WO_3 nanosheets for efficient xylene gas sensing application, J. Alloy. Compd. 826 (2020) 154196, https://doi.org/10.1016/j.jallcom.2020.154196
[13] J. Guo, Y. Li, B. Jiang, H. Gao, T. Wang, P. Sun, F. Liu, Xu Yan, X. Liang, Y. Gao, J. Zhao, G. Lu, Xylene gas sensing properties of hydrothermal synthesized SnO_2-Co_3O_4 microstructure, Sens. Actuators.: B. Chem. 310 (2020) 127780, https://doi.org/10.1016/j.snb.2020.127780
[14] H. Wang, M. Chen, Q. Rong, Y. Zhang, J. Hu, D. Zhang, S. Zhou, X. Zhao, J. Zhang, Z. Zhu, Q. Liu, Ultrasensitive xylene gas sensor based on flower-like SnO_2/Co_3O_4 nanorods composites prepared by facile two-step synthesis method, Nanotechnology 31 (13pp) (2020) 255501, https://doi.org/10.1088/1361-6528/ab70d1
[15] J.-H. Kim, H.-M. Jeong, C.W. Na, J.-W. Yoon, F. Abdel-Hady, A.A. Wazzan, J.-H. Lee, Highly selective and sensitive xylene sensors using Cr_2O_3-$ZnCr_2O_4$ hetero-nanostructures prepared by galvanic replacement, Sens. Actuators B 235 (2016) 498–506, https://doi.org/10.1016/j.snb.2016.05.104
[16] J.F. Chan, J.K. Jeon, Y.K. Moon, J.-H. Lee, Highly sensitive xylene sensors using Fe_2O_3-$ZnFe_2O_4$ composite spheres, J. Sens. Sci. Technol. Vol. 30 (No. 4) (2021) 191–195, https://doi.org/10.46670/JSST.2021.30.4.191
[17] H. Gao, J. Guo, Y. Li, C. Xie, X. Li, L. Liu, Y. Chen, P. Sun, F. Liu, X. Yan, F. Liu, G. Lu, Highly selective and sensitive xylene gas sensor fabricated from NiO/ $NiCr_2O_4$ p-p nanoparticles, Sens. Actuators.: B. Chem. 284 (2019) 305–315, https://doi.org/10.1016/j.snb.2018.12.152
[18] M. Li, W. Xu, R. Jiang, M. Du, L. Zhang, S. Yang, S. Wang, J. Cao, Colloids and Surfaces A: Physicochemical and Engineering Aspects 649 (2022) 129522. https://doi.org/10.1016/j.colsurfa.2022.129522.
[19] X.-T. Xue, L.-Y. Zhu, K.-P. Yuan, C. Zeng, X.-X. Li, H.-P. Ma, H.-L. Lu, D.W. Zhang, ZnO branched p-Cu_xO@n-ZnO heterojunction nanowires for improving acetone gas sensing performance, Sens. Actuators.: B. Chem. 324 (2020) 128729, , https://doi.org/10.1016/j.snb.2020.128729
[20] D.R. Miller, S.A. Akbar, P.A. Morris, Nanoscale metal oxide-based heterojunctions for gas sensing: a review, Sens. Actuators B 204 (2014) 250–272, https://doi.org/10.1016/j.snb.2014.07.074
[21] V.S. Kamble, R.K. Zemase, R.H. Gupta, B.D. Aghav, S.A. Shaikh, J.M. Pawara, S.K. Patil, S.T. Salunkh, Improved toxic NO_2 gas sensing response of Cu-doped ZnO thin-film sensors derived by simple co-precipitation route, Opt. Mater. 131 (2022) 112706, https://doi.org/10.1016/j.optmat.2022.112706
[22] F. Kheiri, V. Soleimanian, M. Ghasemi, A. Mokhtari, The microstructure, optical and gas sensing properties of bilayer TiO_2/ZnO systems in terms of annealing temperature, Mater. Sci. Semicond. Process. 121 (2021) 105462, https://doi.org/10.1016/j.mssp.2020.105462
[23] N. Jamalpoor, M. Ghasemi, V. Soleimanian, Investigation of the role of deposition rate on optical, microstructure and ethanol sensing characteristics of nanostructured Sn doped In_2O_3 films, Mater. Res. Bull. 106 (2018) 49–56, https://doi.org/10.1016/j.materresbull.2018.05.028
[24] R.N. Mariammal, K. Ramachandran, Study on gas sensing mechanism in p-CuO/n-ZnO heterojunction sensor, Mater. Res. Bull. 100 (2018) 420–428, https://doi.org/10.1016/j.materresbull.2017.12.046
[25] R.G. Motsoeneng, I. Kortidis, R. Rikhotso, H.C. Swart, S.S. Ray, D.E. Motaung, Temperature-dependent response to C_3H_7OH and C_2H_5OH vapors induced by deposition of Au nanoparticles on SnO_2/NiO hollow sphere-based conductometric sensors, Sens. Actuators B: Chem. 316 (2020) 128041, https://doi.org/10.1016/j.snb.2020.128041

[26] R. Moradi, R. Yousefi, Z. Adelpour, M. Sadeghi, The effects of Ag concentration on toluene gas sensing performance of Ag NPs decorated on g-C_3N_4 sheets, J. Alloy. Compd. 932 (2023) 167539, https://doi.org/10.1016/j.jallcom.2022.167539
[27] W. Liu, Z. Chen, X. Si, H. Tong, J. Guo, Z. Zhang, J. Huo, G. Cheng, Z. Du, Facile synthesis of Pt catalysts functionalized porous ZnO nanowires with enhanced gas-sensing properties, J. Alloy. Compd. 947 (2023) 169486, https://doi.org/10.1016/j.jallcom.2023.169486
[28] V. Kruefu, A. Wisitsoraat, A. Tuantranont, S. Phanichphant, Ultra-sensitive H_2S sensors based on hydrothermal/impregnation-made Ru-functionalized WO_3 nanorods, Sens. Actuators B 215 (2015) 630–636, https://doi.org/10.1016/j.snb.2015.03.037
[29] X.W. Li, X. Zhou, H. Guo, C. Wang, J.Y. Liu, P. Sun, F.M. Liu, G.Y. Lu, Design of Au@ZnO yolk-shell nanospheres with enhanced gas sensing properties, ACS Appl. Mater. Interfaces 6 (2014) 18661–18667, https://doi.org/10.1021/am5057322
[30] K. Xu, J.P. Zou, S.Q. Tian, Y. Yang, F.Y. Zeng, T. Yu, Y.T. Zhang, X.M. Jie, C.L. Yuan, Single-crystalline porous nanosheets assembled hierarchical Co_3O_4 microspheres for enhanced gas-sensing properties to trace xylene, Sens. Actuators B Chem. 246 (2017) 68–77, https://doi.org/10.1016/j.snb.2017.02.071
[31] H. Gao, J. Guo, Y. Li, C. Xie, X. Li, L. Liu, Y. Chen, P. Sun, F. Liu, X. Yan, F. Liu, G. Lu, Highly selective and sensitive xylene gas sensor fabricated from NiO/$NiCr_2O_4$ p-p nanoparticles, Sens. Actuators: B. Chem. 284 (2019) 305–315, https://doi.org/10.1016/j.snb.2018.12.152
[32] C. Sun, X. Su, F. Xiao, C. Niu, J. Wang, Synthesis of nearly monodisperse Co_3O_4 nanocubes via a microwave-assisted solvothermal process and their gas sensing properties, Sens. Actuators B: Chem. 157 (2011) 681–685, https://doi.org/10.1016/j.snb.2011.05.039
[33] C.Q. Ge, C.S. Xie, S.Z. Cai, Preparation and gas-sensing properties of Ce-doped ZnO thin-film sensors by dip-coating, Mater. Sci. Eng. B 137 (2007) 53–58 06. https://doi:10.1016/j.mseb.2006.10.006.
[34] G.A. Russell, The rates of oxidation of aralkyl hydrocarbons. Polar effects in free radical reactions, J. Am. Chem. Soc. 78 (1956) 1047–1054 https://pubs.acs.org/doi/pdf/10.1021/ja01586a047.
[35] Z.P. Tshabalala, T.P. Mokoena, K.T. Hillie, H.C. Swart, D.E. Motaung, Improved BTEX gas sensing characteristics of thermally treated TiO_2 hierarchical spheres manifested by high-energy {001} crystal facets, Sens. Actuators B: Chem. 338 (2021) 129774, https://doi.org/10.1016/j.snb.2021.129774
[36] P.C. Nam, V.V. Quan, N.M. Thong, P.T.T. Thao, Bond dissociation enthalpies in benzene derivatives and effect of substituents: an overview of density functional theory (B3LYP) based computational approach (International Edition), Vietnam J. Chem. 55 (6) (2017) 679–691, https://doi.org/10.15625/2525-2321.2017-00527
[37] M. Szwarc, The C - C bond energy in ethylbenzene, J. Chem. Phys. 17 (1949) 431–435, https://doi.org/10.1063/1.1747283
[38] L.B. Deng, X.H. Ding, D.W. Zeng, S.P. Zhang, C.S. Xie, High sensitivity and selectivity of C-doped gas sensors toward toluene and xylene, IEEE Sens. J. 12 (2012) 2209–2214, https://doi.org/10.1109/JSEN.2011.2179980
[39] D.L. Baulch, C.T. Bowman, C.J. Cobos, R.A. Cox, T. Just, J.A. Kerr, M.J. Pilling, D. Stocker, J. Troe, W. Tsang, R.W. Walker, J. Warnatz, Evaluated kinetic data for combustion modeling: supplement II, J. Phys. Chem. Ref. Data 34 (2005) 757–1397, https://doi.org/10.1063/1.1748524
[40] M.E. Franke, T.J. Koplin, U. Simon, Metal and metal oxide nanoparticles in chemiresistors: does the nanoscale matter, Small 2 (2006) 36–50, https://doi.org/10.1002/smll.200500261
[41] K. Dutta, P.P. Chattopadhyay, C.W. Lu, M.S. Ho, P. Bhattacharyya, A highly sensitive BTX sensor based on electrochemically derived wall connected TiO_2 nanotubes, Appl. Surf. Sci. 354 (2015) 353–361, https://doi.org/10.1016/j.apsusc.2015.05.077
[42] Y. Xiao, L. Lu, A. Zhang, Y. Zhang, L. Sun, L. Huo, F. Li, Highly enhanced acetone sensing performances of porous and single crystalline ZnO nanosheets: high percentage of exposed (100) facets working together with surface modification with Pd nanoparticles, ACS Appl. Mater. Interfaces 4 (2012) 3797–3804, https://doi.org/10.1021/am3010303
[43] M. Breedon, M.J.S. Spencer, I. Yarovsky, Adsorption of NO_2 on oxygen deficient ZnO ($2\bar{1}\bar{1}0$) for gas sensing applications: a DFT study, J. Phys. Chem. C. 114 (2011) 16603–16610, https://doi.org/10.1021/jp105733p
[44] Z. Lin, M. Xu, P. Fu, Q. Deng, Crystal plane control of 3D iron molybdate and the facet effect on gas sensing performances, Sens. Actuators B: Chem. 254 (2018) 755–762, https://doi.org/10.1016/j.snb.2017.07.101
[45] T.L.H. Doan, J.-Y. Kim, J.-H. Lee, L.H. Thuy Nguyen, H.T. Thu Nguyen, A.T. Thanh Pham, T.B. Nguyen Le, A. Mirzaei, T.B. Phan, S.S. Kim, Facile synthesis of metal-organic framework-derived ZnO/CuO nanocomposites for highly sensitive and selective H_2S gas sensing, Sens. Actuators.: B. Chem. 349 (2021) 130741, https://doi.org/10.1016/j.snb.2021.130741
[46] J.-H. Lee, J.-Y. Kim, J.-H. Kim, A. Mirzaei, H.W. Kim, S.S. Kim, Co_3O_4-loaded ZnO nanofibers for excellent hydrogen sensing, Int. J. Hydrog. Energy 44 (2019) 27499–27510, https://doi.org/10.1016/j.ijhydene.2019.08.226
[47] A. Katoch, S.-W. Choi, J.-H. Kim, J.H. Lee, J.-S. Lee, S.S. Kim, Importance of the nanograin size on the H_2S-sensing properties of ZnO–CuO composite nanofibers, Sens. Actuators B: Chem. 214 (2015) 111–116, https://doi.org/10.1016/j snb.2015.03.012.
[48] Y. Lin, C. Norman, D. Srivastava, F. Azough, L. Wang, M. Robbins, K. Simpson, R. Freer, I.A. Kinloch, Thermoelectric power generation from lanthanum strontium titanium oxide at room temperature through the addition of graphene, ACS Appl. Mater. Interfaces 7 (2015) 15898–15908 https://doi.org/10.1021/ acsami.5b03522.
[49] C.H. Feng, Z.W. Jiang, J.X. Wu, B. Chen, G.Y. Lu, C.Z. Huang, Pt-Cr_2O_3-WO_3 composite nanofibers as gas sensors for ultra-high sensitive and selective xylene detection, Sens. Actuators B 300 (2019) 127008, https://doi.org/10.1016/j.snb.2019.127008
[50] Z.P. Tshabalala, T.P. Mokoena, M. Jozela, J. Tshilongo, T. Hillie, H.C. Swart, D.E. Motaung, TiO_2 nanowires for humidity-stable gas sensors for toluene and Xylene, ACS Appl. Nano Mater. 4 (2021) 702–716, https://doi.org/10.1021/acsanm.0c02963
[51] M. Verma, G. Bahuguna, A. Saharan, S. Gaur, H. Haick, R. Gupta, Room temperature humidity tolerant Xylene sensor using a Sn-SnO_2 nanocomposite, ACS Appl. Mater. Interfaces 15 (15) (2023) 5512–5520, https://doi.org/10.1021/acsami.2c22417
[52] H.P. Wang, M.P. Chen, Q. Rong, Y.M. Zhang, J.C. Hu, D.M. Zhang, S.Q. Zhou, X.B. Zhao, J. Zhang, Z.Q. Zhu, Q.J. Liu, Ultrasensitive xylene gas sensor based on flower-like SnO_2/Co_3O_4 nanorods composites prepared by facile two-step synthesis method, Nanotechnology 31 (2020) 255501, https://doi.org/10.1088/1361-6528/ab70d1
[53] H.Y. Gao, J. Guo, Y.W. Li, C.L. Xie, X. Li, L. Liu, Y. Chen, P. Sun, F.M. Liu, X. Yan, F.M. Liu, G.Y. Lu, Highly selective and sensitive xylene gas sensor fabricated from NiO/$NiCr_2O_4$ p-p nanoparticles, Sens. Actuators B 284 (2019) 305–315, https://doi.org/10.1016/j.snb.2018.12.152
[54] H.Y. Gao, D.D. Wei, P.F. Lin, C. Liu, P. Sun, K. Shimanoe, N. Yamazoe, G.Y. Lu, The design of excellent xylene gas sensor using Sn-doped NiO hierarchical nanostructure, Sens. Actuators B 253 (2017) 1152–1162, https://doi.org/10.1016/j.snb.2017.06.177
[55] J. Guo, Y.W. Li, B. Jiang, H.Y. Gao, T.S. Wang, P. Sun, F.M. Liu, X. Yan, X.S. Liang, Y. Gao, J. Zhao, G.Y. Lu, Xylene gas sensing properties of hydrothermal synthesized SnO_2-Co_3O_4 microstructure, Sens. Actuators B 310 (2020) 127780, https://doi.org/10.1016/j.snb.2020.127780
[56] Y. Shi, T. Liu, Y. Zhao, J. Su, S. Zeb, Y. Nie, C. Qin, B. Wang, X. Jiang, Tunable oxygen vacancies of cobalt oxides for efficient gas sensing application, Sens. Actuators.: B. Chem. 350 (2022) 130860, https://doi.org/10.1016/j.snb.2021.130860
[57] O. Mnethu, S.S. Nkosi, I. Kortidis, D.E. Motaung, R.E. Kroon, H.C. Swart, N.G. Ntsasa, J. Tshilongo, T. Moyo, Ultra-sensitive and selective p-xylene gas sensor at low operating temperature utilizing Zn doped CuO nanoplatelets: insignificant vestiges of oxygen vacancies, J. Colloids Interface Sci. 576 (2020) 364–375, https://doi.org/10.1016/j.jcis.2020.05.030
[58] L. Teng, Y. Liu, M. Ikram, Z. Liu, M. Ullah, L. Ma, X. Zhang, H. Wu, L. Li, K. Shi, One-step synthesis of palladium oxide-functionalized tin dioxide nanotubes: characterization and high nitrogen dioxide gas sensing performance at room temperature, J. Colloid Interface Sci. 537 (2019) 79–90, https://doi.org/10.1016/j.jcis.2018.11.001
[59] Z. Zhu, Z.-X. Chiang, R.-J. Wu, U. Kumar, C.-H. Wu, A combined experimental and theoretical study of composite SnO_2–$BiVO_4$ for selective NO_2 sensing, Mater. Chem. Phys. 292 (2022) 126868, https://doi.org/10.1016/j.matchemphys.2022.126868
[60] T.P. Mokoena, H.C. Swart, K.T. Hillie, Z.P. Tshabalala, M. Jozela, J. Tshilongo, D.E. Motaung, Enhanced propanol gas sensing performance of p-type NiO gas sensor induced by exceptionally large surface area and crystallinity, Appl. Surf. Sci. 571 (2022) 151121, https://doi.org/10.1016/j.apsusc.2021.151121
[61] R. Kumar, N. Goel, M. Kumar, High performance NO_2 sensor using MoS_2 nanowires network, Appl. Phys. Lett. 112 (2018) 53502, https://doi.org/10.1063/1.5019296
[62] Z. Liu, H. Lv, Y. Xie, J. Wang, J. Fan, B. Sun, L. Jiang, Y. Zhang, R. Wang, K. Shi, A, 2D/2D/2D Ti_3C_2Tx@TiO_2@MoS_2 heterostructure as an ultrafast and high sensitivity NO_2 gas sensor at room-temperature, J. Mater. Chem. A (2022), https://doi.org/10.1039/D1TA09369J
[63] Qui Thanh Hoai Ta, Nguyen Ngoc Tri, Jin-Seo Noh, Improved NO_2 gas sensing performance of 2D MoS_2/$Ti_3C_2T_x$ MXene nanocomposite, Appl. Surf. Sci. 604 (2022) 154624, , https://doi.org/10.1016/j.apsusc.2022.154624
[64] H. Fang, S. Li, H. Zhao, J. Deng, D. Wang, J. Li, Enhanced NO_2 gas sensing performance by hierarchical CuO–Co_3O_4 spheres, Sens. Actuators.: B. Chem. 352 (2022) 131068, https://doi.org/10.1016/j.snb.2021.131068
[65] D.N. Oosthuizen, I. Kortidis, H.C. Swart, D.E. Motaung, Facile control of room temperature nitrogen dioxide gas selectivity induced by copper oxide nanoplatelets, J. Colloid Interface Sci. 560 (2020) 755–768, https://doi.org/10.1016/j.jcis.2019.10.036
[66] Z. Li, L. Guo, Z. Feng, S. Gao, H. Zhang, X. Yang, H. Liu, J. Shao, C. Sun, Y. Cheng, G. Pan, Metal-organic framework-derived ZnO decorated with CuO for ultra-high response and selectivity H_2S gas sensor, Sens. Actuators.: B. Chem. 366 (2022) 131995, https://doi.org/10.1016/j.snb.2022.131995
[67] S. Hussain, J.N. Okai Amu-Darko, M. Wang, A.A. Alothman, M. Ouladsmane, S.A. Aldossari, M.S. Khan, G. Qiao, G. Liu, CuO-decorated MOF derived ZnO polyhedral nanostructures for exceptional H_2S gas detection, Chemosphere 317 (2023) 137827, https://doi.org/10.1016/j.chemosphere.2023.137827
[68] S. Oh, J.-S. Park, H.-J. Lee, H.M. Jeong, Selective acetone gas sensing of $Cu_2(OH)_3F$/CuO enhanced by hydroxy bonds and fluorine substitution, Sens. Actuators: B. Chem. 372 (2022) 132662, https://doi.org/10.1016/j.snb.2022.132662
[69] M. Al-Hashem, S. Akbar, P. Morris, Role of oxygen vacancies in nanostructured metal-oxide gas sensors: a review, Sens. Actuator B: Chem. 301 (2019) 24, https://doi.org/10.1016/j.snb.2019.126845